J Sci Comput (2007) 33: 47–74
DOI 10.1007/s10915-007-9143-y

Dispersion and Dissipation Error in High-Order Runge-Kutta Discontinuous Galerkin Discretisations of the Maxwell Equations

D. Sármány · M.A. Botchev · J.J.W. van der Vegt

Received: 21 December 2006 / Accepted: 13 June 2007 / Published online: 14 July 2007

Abstract Different time-stepping methods for a nodal high-order discontinuous Galerkin discretisation of the Maxwell equations are discussed. A comparison between the most popular choices of Runge-Kutta (RK) methods is made from the point of view of accuracy and computational work. By choosing the strong-stability-preserving Runge-Kutta (SSP-RK) time-integration method of order consistent with the polynomial order of the spatial discretisation, better accuracy can be attained compared with fixed-order schemes. Moreover, this comes without a significant increase in the computational work. A numerical Fourier analysis is performed for this Runge-Kutta discontinuous Galerkin (RKDG) discretisation to gain insight into the dispersion and dissipation properties of the fully discrete scheme. The analysis is carried out on both the one-dimensional and the two-dimensional fully discrete schemes and, in the latter case, on uniform as well as on non-uniform meshes. It also provides practical information on the convergence of the dissipation and dispersion error up to polynomial order 10 for the one-dimensional fully discrete scheme.

Keywords High-order nodal discontinuous Galerkin methods · Maxwell equations · Numerical dispersion and dissipation · Strong-stability-preserving Runge-Kutta methods

1 Introduction

As pointed out in an extensive review on the state of the art of computational electromagnetics [16], in many cases finite-difference time-domain (FDTD) schemes [33, 37] are

D. Sármány (✉) · M.A. Botchev · J.J.W. van der Vegt
Department of Applied Mathematics, University of Twente, P.O. Box 217, 7500 AE Enschede, Netherlands
e-mail: d.sarmany@math.utwente.nl

M.A. Botchev
e-mail: m.a.botchev@math.utwente.nl

J.J.W. van der Vegt
e-mail: j.j.w.vandervegt@math.utwente.nl

undoubtedly the most popular methods among physicists and engineers to solve the time-domain Maxwell equations numerically. This popularity is mainly due to their simplicity and efficiency in discretising simple-domain problems. However, their inability to effectively handle complex geometries prompted some scientists to search for alternatives long ago. Finite-element (FE) methods are an obvious alternative, but early efforts were marred by the fact that standard continuous Galerkin finite-element schemes give rise to non-physical solutions. Most apparent of these are the spurious modes in the numerical solution of the frequency-domain Maxwell equations (see [24] and references therein). The revolutionary solution to this problem was to realise that by using a particular set of vector basis functions (vector elements such as Nédélec or Whitney elements [20, 29]), it is possible to mimic many of the special properties of the Maxwell equations at the discrete level. See [3] and [4]. Ever since, vector elements have been a viable alternative to FDTD and standard FE methods in computational electrodynamics, especially for frequency-domain problems with complex geometries. The practical considerations of both standard and vector finite elements in computational electromagnetics are covered in [24]. For the more theoretical aspects of Nédélec elements we refer to [27].

The need to model electromagnetic wave propagation in large and complex domains and over a relatively long time span has increased the demand for high-order methods. However, neither high-order FDTD methods nor high-order vector FE methods are devoid of practical drawbacks. High-order FDTD methods fail to effectively handle complex geometries whereas high-order vector FE methods (based on high-order Nédélec elements [29] for example) lead to global mass matrices with relatively large bandwidths (after optimal reordering). The time-integration schemes to solve such systems are in turn computationally rather expensive. These difficulties have motivated the development of discontinuous Galerkin (DG) finite-element methods [9, 11], together with spectral element methods [25]. In both the frequency-domain formulation [19, 21, 30, 31, 35] and the time-domain formulation [6, 10, 18, 28] significant progress has been made. One of the most promising methods for complicated geometries is the high-order nodal DG method of Hesthaven and Warburton [18], which proved both accurate and efficient for the spatial discretisation. In time integration, however, the low-storage Runge-Kutta (RK) method the authors applied poses a comparatively stringent time-step constraint, which may turn out to be the bottleneck for long-time integration. Furthermore, fixed-order time-integration schemes may spoil the high-order convergence of the global scheme. In the meantime, for discontinuous formulations of convection-dominated problems [9] it has been shown in [14] and in [6] that the time-step restriction may be loosened if we use Strong-Stability-Preserving Runge-Kutta (SSP-RK) methods of one order higher than the polynomial order of the spatial discretisation.

In this work, we study the behaviour of the high-order nodal scheme when several of the best-suited time-integration methods are used. In particular, we have a closer look at the dispersion and dissipation properties of the Runge-Kutta discontinuous Galerkin (RKDG) method comprising the nodal high-order DG method and the SSP-RK method. The main motivation for using this particular time-integration scheme is its relatively weak time-step restriction. This property implies that we can retain high-order accuracy without losing much on the computational work measured as the number of operations.

The literature on the dispersion and dissipation properties of the DG method has in recent years become abundant. A thorough analysis of the dispersion and dissipation behaviour of the DG method for the transport equation (scalar linear conservation law) was given in [1], which also provided a proof for earlier conjectures, especially from [22]. The semi-discrete system for the wave equation has also been extensively studied [2, 23, 32]. In particular, the

authors in [2] provided two different dispersion analyses for the semi-discrete wave equation on tensor product elements. One for the interior penalty DG method (IP-DG) of the second-order wave equation and another for the general DG method for a first order system.

The novelty of this work with regards to the dispersion and dissipation behaviour of DG methods lies in including the time integration in the analysis. We consider the discretisation of the first-order system related to the Maxwell equations, so our scheme falls in the category of what the authors call the 'general DG method' in [2]. Throughout this article we apply a fully upwinding numerical flux, since it has proved superior—due to stabilisation and lack of spurious modes—to the centered or mixed fluxes for time-dependent problems [19]. In wave-propagation problems it is often more advantageous to know the convergence rate of the dispersion and dissipation errors than that of the error in the L_2-norm. These convergence rates have been established in [1] for the semi-discrete transport equation. For the general DG scheme, to which the nodal DG method discussed here belongs, it has been shown in [2] that using first-order polynomials in the spatial discretisation results in a dispersion error of order $\mathcal{O}(h^4)$ and a dissipation error of order $\mathcal{O}(h^3)$ for the semi-discrete system. In this work we show, through numerical examples, how the dispersion and dissipation errors converge in the fully discrete high-order RKDG scheme for the linear autonomous form of the Maxwell equations.

The remaining part of this article is outlined as follows. In Sect. 2 we recall the system of time-domain Maxwell equations and reduce it to the linear autonomous form. The spatial discretisation is briefly reviewed in Sect. 3 and the RK schemes for the temporal discretisation in Sect. 4. One-dimensional and two-dimensional Fourier analysis is carried out in Sect. 5, and the associated numerical results, along with some other numerical tests, are presented in Sect. 6. Here we examine the behaviour of the dispersion and dissipation errors in terms of the mesh size per wave length and the size of the time step. Finally, we sum up our conclusions in Sect. 7.

2 Maxwell Equations

We begin with deriving the dimensionless time-domain form of the Maxwell equations in the three-dimensional domain $\Omega \subset \mathbb{R}^3$. Boldface symbols here refer to vector fields, i.e. fields in $\mathbb{R}^3 \to \mathbb{R}^3$. With these notations the Maxwell equations read

$$\frac{\partial \boldsymbol{D}}{\partial t} = \nabla \times \boldsymbol{H} - \boldsymbol{J}, \qquad \frac{\partial \boldsymbol{B}}{\partial t} = -\nabla \times \boldsymbol{E}, \tag{1}$$

$$\nabla \cdot \boldsymbol{D} = \varrho, \qquad \nabla \cdot \boldsymbol{B} = 0, \tag{2}$$

with charge distribution $\varrho(\boldsymbol{x}, t)$, position vector $\boldsymbol{x} = (x, y, z) \in \Omega$, the nabla operator $\nabla = (\frac{\partial}{\partial x}, \frac{\partial}{\partial y}, \frac{\partial}{\partial z})$ and time t. The vector valued quantities are the electric field $\boldsymbol{E}(\boldsymbol{x}, t)$, the electric flux density $\boldsymbol{D}(\boldsymbol{x}, t)$, the magnetic field $\boldsymbol{H}(\boldsymbol{x}, t)$, the magnetic flux density $\boldsymbol{B}(\boldsymbol{x}, t)$ and the electric current $\boldsymbol{J}(\boldsymbol{x}, t)$. For many applications it is reasonable to assume that the materials are isotropic, linear and time-invariant. Thus the system of equations is closed with the linear constitutive relations

$$\boldsymbol{D} = \varepsilon_{\mathrm{r}} \boldsymbol{E}, \qquad \boldsymbol{B} = \mu_{\mathrm{r}} \boldsymbol{H}, \tag{3}$$

where the scalar quantities $\varepsilon_{\mathrm{r}}(\boldsymbol{x})$ and $\mu_{\mathrm{r}}(\boldsymbol{x})$ are the permittivity and permeability, respectively. Furthermore, Ohm's law

$$\boldsymbol{J} = \sigma \boldsymbol{E}$$

also holds with electric conductivity $\sigma(\boldsymbol{x}, t)$.

To obtain the non-dimensional form of the Maxwell equations (1–2), we first introduce tilded variables to represent the dimensional fields. The special notations $\tilde{\varepsilon}_0$ and $\tilde{\mu}_0$ stand for the dimensional permittivity and permeability of vacuum. By using the normalised space and time variables

$$\boldsymbol{x} = \frac{\tilde{\boldsymbol{x}}}{\tilde{L}}, \qquad t = \frac{\tilde{t}}{\tilde{L}/\tilde{c}_0},$$

with reference length $\tilde{L}$ and dimensional speed of light in vacuum $\tilde{c}_0 = 1/\sqrt{\tilde{\varepsilon}_0\tilde{\mu}_0}$, the physical fields are made non-dimensional through the relations

$$\boldsymbol{E} = \frac{\tilde{\boldsymbol{E}}}{\tilde{Z}_0\tilde{H}_0}, \qquad \boldsymbol{H} = \frac{\tilde{\boldsymbol{H}}}{\tilde{H}_0}, \qquad \boldsymbol{J} = \frac{\tilde{\boldsymbol{J}}}{\tilde{H}_0/\tilde{L}}.$$

Here $\tilde{Z}_0 = \sqrt{\tilde{\mu}_0/\tilde{\varepsilon}_0}$ and $\tilde{H}_0$ are the free-space intrinsic impedance and reference magnetic field strength, respectively.

With the constitutive relations (3), (2) are just the consistency conditions for (1). To see that point, we only need to take the divergence of (1), apply (2) and (3) and realise that the resultant equation represents nothing else but charge conservation, which should always hold. Consequently, as long as the initial conditions satisfy (2) and the fields evolve according to (1), the solution at any time will also satisfy (2). It is therefore enough to consider only

$$\varepsilon_{\mathrm{r}}\frac{\partial \boldsymbol{E}}{\partial t} = \nabla \times \boldsymbol{H} - \boldsymbol{J}, \qquad \mu_{\mathrm{r}}\frac{\partial \boldsymbol{H}}{\partial t} = -\nabla \times \boldsymbol{E}, \tag{4}$$

in which the constitutive relations (3) are also included. As for the boundary conditions, one important special case is that of perfect electric conductors (PEC). These read

$$\hat{\boldsymbol{n}} \times \boldsymbol{E} = 0, \qquad \hat{\boldsymbol{n}} \times \boldsymbol{H} = 0, \tag{5}$$

with outward pointing normal vector $\hat{\boldsymbol{n}}$. Between material interfaces, in the absence of surface currents and surface charge, the following conditions are valid

$$\begin{aligned} \hat{\boldsymbol{n}} \times [\![\boldsymbol{E}]\!] &= 0, \qquad \hat{\boldsymbol{n}} \cdot [\![\varepsilon_r \boldsymbol{E}]\!] = 0, \\ \hat{\boldsymbol{n}} \times [\![\boldsymbol{H}]\!] &= 0, \qquad \hat{\boldsymbol{n}} \cdot [\![\mu_r \boldsymbol{H}]\!] = 0, \end{aligned} \tag{6}$$

where

$$[\![\boldsymbol{u}]\!] = \boldsymbol{u}^+ - \boldsymbol{u}^-$$

denotes the jump in the field value $\boldsymbol{u}$. The expressions (6) represent the physical property that the tangential components of both fields are continuous across different materials, whereas the normal components may be discontinuous.

3 Discontinuous Galerkin Discretisation in Space

We approximate the solutions to the Maxwell equations in space using the high-order nodal discontinuous Galerkin method introduced in [18] and further studied in [19] and [35]. In the following we briefly review the main features of this discretisation.

We consider the Maxwell equations in the general domain $\Omega \subset \mathbb{R}^3$ filled with non-conductive materials ($\sigma = 0$) and rewrite (4) in the flux form

$$Q(\boldsymbol{x})\frac{\partial \boldsymbol{q}}{\partial t} + \nabla \cdot \boldsymbol{F}(\boldsymbol{q}) = 0, \tag{7}$$

where $Q(\boldsymbol{x})$ represents the material properties, $\boldsymbol{q}$ is the vector of the field values and $\boldsymbol{F}(\boldsymbol{q}) = [F_1(\boldsymbol{q}), F_2(\boldsymbol{q}), F_3(\boldsymbol{q})]^T$ denotes the flux. Namely,

$$Q(\boldsymbol{x}) = \mathtt{diag}(\varepsilon_{\mathrm{r}}, \varepsilon_{\mathrm{r}}, \varepsilon_{\mathrm{r}}, \mu_{\mathrm{r}}, \mu_{\mathrm{r}}, \mu_{\mathrm{r}}), \qquad \boldsymbol{q} = \begin{bmatrix} \boldsymbol{E} \\ \boldsymbol{H} \end{bmatrix}, \qquad F_i(\boldsymbol{q}) = \begin{bmatrix} -\boldsymbol{e}_i \times \boldsymbol{H} \\ \boldsymbol{e}_i \times \boldsymbol{E} \end{bmatrix},$$

where $\boldsymbol{e}_i$ is the corresponding Cartesian unit vector. We seek the numerical solution in the computational domain Ω_K tessellated into K non-overlapping elements, i.e.

$$\Omega \approx \Omega_K = \bigcup_{k=1}^{K} \Omega^k.$$

Here Ω_K represents a tetrahedral tessellation in three dimensions and a triangular tessellation in two dimensions.

Before formulating the discontinuous Galerkin discretisation, we introduce the standard (or reference) element $\Omega_{\mathrm{st}} = \mathcal{T}^d$ for different spatial dimensions d. These are defined as $\mathcal{T}^1 = \{\xi : -1 \le \xi \le 1\}$ in one dimension, $\mathcal{T}^2 = \{\boldsymbol{\xi} = (\xi, \eta) : -1 \le \xi, \eta, \xi + \eta \le 0\}$ in two dimensions and $\mathcal{T}^3 = \{\boldsymbol{\xi} = (\xi, \eta, \zeta) : -1 \le \xi, \eta, \zeta, \xi + \eta + \zeta \le -1\}$ in three dimensions. Each element Ω^k is constructed by the invertible mapping $\mathcal{X}^k(\boldsymbol{\xi}) : \Omega_{\mathrm{st}} \to \Omega^k$, which is unique for any given element. For details see the extensive book [25]. We now define the finite element space as

$$\mathcal{V}_h = \left\{ \boldsymbol{q}_N^k \in (L^2(\Omega))^{2\mathrm{d}} : \boldsymbol{q}_N^k(\mathcal{X}^k(\xi)) \in \mathcal{P}_p^d(\Omega_{\mathrm{st}}),\ k = 1, \ldots, K \right\}, \tag{8}$$

where $L^2(\Omega)$ is the space of square integrable functions on Ω and $\mathcal{P}_p^d(\Omega_{\mathrm{st}})$ denotes the space of d-dimensional polynomials of maximum order p on the reference element Ω_{st}. Since this polynomial space is associated with

$$N = \frac{(n+d)!}{n!\,d!}$$

nodal points $\boldsymbol{\xi}_i \in \Omega_{\mathrm{st}}$, we can now introduce the multidimensional Lagrange polynomials $L_i(\boldsymbol{\xi})$ passing through these nodes:

$$L_i(\boldsymbol{\xi}_j) = \delta_{ij}, \quad \text{with } \delta_{ij} = \begin{cases} 1 & \text{if } i = j, \\ 0 & \text{if } i \neq j. \end{cases}$$

Taking the Lagrange polynomials as trial functions and using the mapping $\mathcal{X}^k(\xi)$, we approximate the solution at the N nodal points within each element as

$$\boldsymbol{q}^k(\boldsymbol{x}, t) \approx \boldsymbol{q}_N^k(\boldsymbol{x}, t) = \sum_{i=1}^{N} \boldsymbol{q}_i^k(t)(L_i(\boldsymbol{x}))^{2\mathrm{d}} \in \mathcal{P}_p^d(\Omega^k),$$

where $\boldsymbol{q}_N^k(\boldsymbol{x}, t)$ is the finite element approximation, and $\boldsymbol{q}_i^k(t)$ represents the solution at nodal point $\boldsymbol{x}_j \in \Omega^k$.

The distribution of the nodes is a key issue for the properties of the interpolation, especially for very high-order approximations. It is best measured by the Lebesgue constant associated with the Lagrange polynomials going through a particular set of nodes. The Lebesgue constant shows just how close a given polynomial approximation is to the best polynomial approximation. The most popular choices for nodes in spectral/hp element methods are the Fekete points [34] and the electrostatic points [15, 17]. It should be noted that although the Fekete points have the best interpolation properties (lowest Lebesgue constant) in a triangle for orders $p \geq 9$, no distribution for a tetrahedron has so far been provided. An (almost) optimal distribution of the electrostatic nodes, however, is given for a triangle in [15] and for a tetrahedron in [17]. Moreover, the electrostatic points also perform slightly better for orders $p \leq 8$ in triangles. The distribution of these nodes in the standard triangle is shown in Fig. 1 for orders $p = 2, 4, 6, 10$. We also note that the nodal distributions in a triangle and tetrahedron with an L^2-norm optimal Lebesgue constant were determined in [7] and [8]. However, these nodes, in contrast with the Fekete and electrostatic points, do not have an

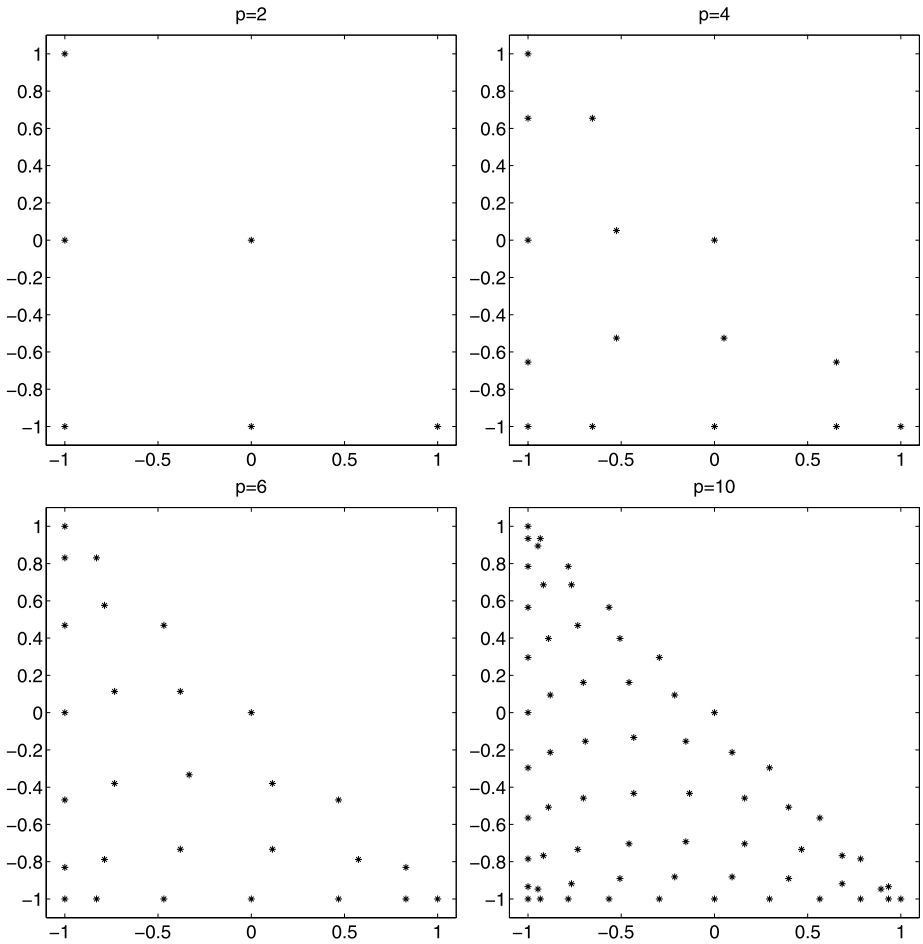

Fig. 1 Electrostatic points for orders $p = 2, 4, 6, 10$

edge distribution which can be identified with Gauss-Lobatto-Jacobi points. We refer to [25] for further overview on nodal (and modal) spectral/hp methods.

To formulate the discontinuous Galerkin scheme, we first introduce the local inner product and its associated norm on Ω^k as

$$(\boldsymbol{u}, \boldsymbol{v})_{\Omega^k} = \int_{\Omega^k} \boldsymbol{u} \cdot \boldsymbol{v} \, \mathrm{d}\boldsymbol{x}, \qquad \|\boldsymbol{u}\|^2_{\Omega^k} = (\boldsymbol{u}, \boldsymbol{u})_{\Omega^k}$$

and on its boundary $\partial\Omega^k$ as

$$(\boldsymbol{u}, \boldsymbol{v})_{\partial\Omega^k} = \int_{\partial\Omega^k} \boldsymbol{u} \cdot \boldsymbol{v} \, \mathrm{d}\boldsymbol{s}.$$

We multiply (7) with the local test function $\phi \in \mathcal{P}^d_p(\Omega^k)$, chosen to be the same interpolating Lagrange polynomials $L_i(\boldsymbol{x})$ as for the trial basis functions, drop the superscript k and integrate by parts over element Ω^k to obtain the continuous weak formulation

$$\left(Q \frac{\partial \boldsymbol{q}}{\partial t}, \phi \right)_{\Omega^k} - (\boldsymbol{F}, \nabla\phi)_{\Omega^k} = -(\hat{\boldsymbol{n}} \cdot \boldsymbol{F}, \phi)_{\partial\Omega^k}, \quad \forall \Omega^k \subset \Omega_K. \tag{9}$$

We then replace the continuous variable $\boldsymbol{q}$ with its discrete counterpart $\boldsymbol{q}_N$, and the exact flux $\boldsymbol{F}$ with the numerical flux $\widehat{\boldsymbol{F}}$ to account for the multi-valued traces at the element boundary. Finally, integration by parts for the second time results in the discrete formulation

$$\left(Q \frac{\partial \boldsymbol{q}_N}{\partial t} + \nabla \boldsymbol{F}_N, \phi \right)_{\Omega^k} = (\hat{\boldsymbol{n}} \cdot [\boldsymbol{F} - \widehat{\boldsymbol{F}}], \phi)_{\partial\Omega^k}. \tag{10}$$

The right-hand side of (10) is responsible for the communication between the elements through the numerical flux $\widehat{\boldsymbol{F}}$. The role of the numerical flux in the present spatial discretisation is discussed in [19] in the light of the Maxwell eigenvalue problem. Throughout this work, we use the upwind flux [26], where information travels along local wave directions.

In order to formulate the upwind flux, we first introduce the impedance Z and the conductance Y defined as

$$Z = Y^{-1} = \sqrt{\mu_\mathrm{r}/\varepsilon_\mathrm{r}}.$$

We also introduce the associated quantities

$$Z^\pm = \frac{1}{Y^\pm} = \sqrt{\frac{\mu^\pm_\mathrm{r}}{\varepsilon^\pm_\mathrm{r}}}, \qquad \bar{Z} = \frac{Z^- + Z^+}{2}, \qquad \bar{Y} = \frac{Y^- + Y^+}{2}.$$

The upwind flux at dielectric interfaces then reads as

$$\hat{\boldsymbol{n}} \cdot \widehat{\boldsymbol{F}} = \frac{1}{2} \begin{bmatrix} \bar{Z}^{-1}(-\hat{\boldsymbol{n}} \times Z^- \boldsymbol{H}^-_N - \hat{\boldsymbol{n}} \times Z^+ \boldsymbol{H}^+_N + \hat{\boldsymbol{n}} \times \hat{\boldsymbol{n}} \times [\![\boldsymbol{E}_N]\!]) \\ \bar{Y}^{-1}(\hat{\boldsymbol{n}} \times Y^- \boldsymbol{E}^-_N + \hat{\boldsymbol{n}} \times Y^+ \boldsymbol{E}^+_N + \hat{\boldsymbol{n}} \times \hat{\boldsymbol{n}} \times [\![\boldsymbol{H}_N]\!]) \end{bmatrix}, \tag{11}$$

where $(\boldsymbol{E}^-_N, \boldsymbol{H}^-_N)$ and $(\boldsymbol{E}^+_N, \boldsymbol{H}^+_N)$ denote the local and neighbouring solution at the boundary of Ω^k, respectively. We emphasise that the cross product is defined between vectors at each node of the element. For a detailed derivation of the upwind flux we refer to [26]. We should also recognise that

$$\hat{\boldsymbol{n}} \cdot \boldsymbol{F}_N = \begin{bmatrix} -\hat{\boldsymbol{n}} \times \boldsymbol{H}^-_N \\ \hat{\boldsymbol{n}} \times \boldsymbol{E}^-_N \end{bmatrix},$$

and combining this with (11), the penalising boundary term will now read

$$\hat{\boldsymbol{n}} \cdot (\boldsymbol{F}_N - \widehat{\boldsymbol{F}}) = \frac{1}{2} \begin{bmatrix} \bar{Z}^{-1}(Z^+ \hat{\boldsymbol{n}} \times [\![\boldsymbol{H}_N]\!] - \hat{\boldsymbol{n}} \times \hat{\boldsymbol{n}} \times [\![\boldsymbol{E}_N]\!]) \\ \bar{Y}^{-1}(-Y^+ \hat{\boldsymbol{n}} \times [\![\boldsymbol{E}_N]\!] - \hat{\boldsymbol{n}} \times \hat{\boldsymbol{n}} \times [\![\boldsymbol{H}_N]\!]) \end{bmatrix}.$$

To obtain the semi-discrete system we introduce the N-by-N local mass and stiffness matrices as

$$\begin{aligned} \mathbf{M}_{ij} &= (L_i(\boldsymbol{x}), L_j(\boldsymbol{x}))_{\Omega^k}, & \mathbf{S}^x_{ij} &= (L_i(\boldsymbol{x}), \partial_x L_j(\boldsymbol{x}))_{\Omega^k}, \\ \mathbf{S}^y_{ij} &= (L_i(\boldsymbol{x}), \partial_y L_j(\boldsymbol{x}))_{\Omega^k}, & \mathbf{S}^z_{ij} &= (L_i(\boldsymbol{x}), \partial_z L_j(\boldsymbol{x}))_{\Omega^k}, \end{aligned} \tag{12}$$

and the face-based mass matrices

$$\mathbf{F}_{il} = (L_i(\boldsymbol{x}), L_l(\boldsymbol{x}))_{\partial\Omega^k}, \tag{13}$$

where the second index is limited to the boundaries of Ω^k.

We can now express the semi-discrete scheme as the following system of ordinary differential equations

$$\begin{aligned} \frac{\mathrm{d}E^x_N}{\mathrm{d}t} &= (\varepsilon_\mathrm{r}\mathbf{M})^{-1}(\mathbf{S}^y H^z_N - \mathbf{S}^z H^y_N) + (\varepsilon_\mathrm{r}\mathbf{M})^{-1}\mathbf{F}\left(\hat{\boldsymbol{n}} \times \frac{Z^+[\![\boldsymbol{H}_N]\!] - \hat{\boldsymbol{n}} \times [\![\boldsymbol{E}_N]\!]}{Z^+ + Z^-}\right)^x\Big|_{\partial\Omega^k}, \\ \frac{\mathrm{d}E^y_N}{\mathrm{d}t} &= (\varepsilon_\mathrm{r}\mathbf{M})^{-1}(\mathbf{S}^z H^x_N - \mathbf{S}^x H^z_N) + (\varepsilon_\mathrm{r}\mathbf{M})^{-1}\mathbf{F}\left(\hat{\boldsymbol{n}} \times \frac{Z^+[\![\boldsymbol{H}_N]\!] - \hat{\boldsymbol{n}} \times [\![\boldsymbol{E}_N]\!]}{Z^+ + Z^-}\right)^y\Big|_{\partial\Omega^k}, \\ \frac{\mathrm{d}E^z_N}{\mathrm{d}t} &= (\varepsilon_\mathrm{r}\mathbf{M})^{-1}(\mathbf{S}^x H^y_N - \mathbf{S}^y H^x_N) + (\varepsilon_\mathrm{r}\mathbf{M})^{-1}\mathbf{F}\left(\hat{\boldsymbol{n}} \times \frac{Z^+[\![\boldsymbol{H}_N]\!] - \hat{\boldsymbol{n}} \times [\![\boldsymbol{E}_N]\!]}{Z^+ + Z^-}\right)^z\Big|_{\partial\Omega^k}, \end{aligned} \tag{14}$$

$$\begin{aligned} \frac{\mathrm{d}H^x_N}{\mathrm{d}t} &= (\varepsilon_\mathrm{r}\mathbf{M})^{-1}(\mathbf{S}^z E^y_N - \mathbf{S}^y E^z_N) + (\varepsilon_\mathrm{r}\mathbf{M})^{-1}\mathbf{F}\left(\hat{\boldsymbol{n}} \times \frac{Y^+[\![\boldsymbol{E}_N]\!] + \hat{\boldsymbol{n}} \times [\![\boldsymbol{H}_N]\!]}{Y^+ + Y^-}\right)^x\Big|_{\partial\Omega^k}, \\ \frac{\mathrm{d}H^y_N}{\mathrm{d}t} &= (\varepsilon_\mathrm{r}\mathbf{M})^{-1}(\mathbf{S}^x E^z_N - \mathbf{S}^z E^x_N) + (\varepsilon_\mathrm{r}\mathbf{M})^{-1}\mathbf{F}\left(\hat{\boldsymbol{n}} \times \frac{Y^+[\![\boldsymbol{E}_N]\!] + \hat{\boldsymbol{n}} \times [\![\boldsymbol{H}_N]\!]}{Y^+ + Y^-}\right)^y\Big|_{\partial\Omega^k}, \\ \frac{\mathrm{d}H^z_N}{\mathrm{d}t} &= (\varepsilon_\mathrm{r}\mathbf{M})^{-1}(\mathbf{S}^y E^x_N - \mathbf{S}^x E^y_N) + (\varepsilon_\mathrm{r}\mathbf{M})^{-1}\mathbf{F}\left(\hat{\boldsymbol{n}} \times \frac{Y^+[\![\boldsymbol{E}_N]\!] + \hat{\boldsymbol{n}} \times [\![\boldsymbol{H}_N]\!]}{Y^+ + Y^-}\right)^z\Big|_{\partial\Omega^k}. \end{aligned} \tag{15}$$

Here the fields E^x_N, E^y_N, E^z_N, H^x_N, H^y_N, and H^z_N represent the discrete counterparts of *scalar* fields. That is the reason they are not typeset boldface, despite now being in fact vectors as a result of the discretisation. In contrast, we evaluate the numerical flux in the right-hand side of (14–15) at each node at the boundary of the element using the discrete counterparts of *vector* fields. Then at each node the corresponding component of the resulting vector is taken.

The advantages of the above described discretisation are discussed in detail in [18] and [35], where a number of numerical examples are also provided. Here it suffices to mention its optimal flexibility for mesh refinement, the possibility of independent adjustment of polynomial orders in each element (hp-adaptation), its excellent performance on parallel computers and that only matrix-matrix multiplications are needed during the time integration. In this article, however, our aim is to analyse the properties of time-integration methods

suitable for this spatial DG discretisation, therefore we assemble the local semi-discrete system (14–15) into a global matrix and consider the 'abstract' semi-discrete system

$$\frac{\mathrm{d}\boldsymbol{q}_h}{\mathrm{d}t} = \boldsymbol{\mathcal{A}}\boldsymbol{q}_h, \tag{16}$$

where $\boldsymbol{\mathcal{A}}$ is the global matrix and $\boldsymbol{q}_h = [\boldsymbol{E}_h, \boldsymbol{H}_h]^T$ represents the numerical approximation to the fields in the complete domain. The matrix assembly is somewhat lengthy but straightforward, and it follows the standard procedure. See [25] for example.

4 Runge-Kutta Time-Stepping Methods

From the point of view of time integration, one of the main difficulties in high-order spectral/hp element methods is the restriction on the time step of explicit time-integration schemes. For hyperbolic systems in general, and for the advection equation in particular, it is known (see [25], for example) that the maximum eigenvalue of the semi-discrete global matrix grows as $\mathcal{O}(p^2)$ with polynomial order p, hence the time step is usually bounded by $\mathcal{O}(1/p^2)$. The time-step restriction then can generally be taken as

$$\Delta t \leq \Delta t_{\max} = \mathrm{CFL}(p)\frac{h_k}{c_k}, \tag{17}$$

where h_k is the minimum edge length of all elements and c_k is the maximum wave speed in the domain. Here the parameter CFL depends on the degree of the polynomials used in the spatial discretisation. If we apply any given time-integration scheme with fixed order (i.e. independent of the polynomial order p) to the semi-discrete system (16), we have

$$\mathrm{CFL}(p) = \mathrm{C}\frac{1}{p^2}, \tag{18}$$

where C is a constant, typically of order one. This condition may turn out to be rather restrictive as we go to higher and higher order approximations, even with a slightly increasing value for C (see Sect. 6).

The low-storage Runge-Kutta schemes introduced in [5] are among the most popular choices for time integration of the DG space-discretised Maxwell equations. Storage can be essential for large-scale computations and low-storage schemes require only two storage units per ODE variable. If we consider the ODE system

$$\frac{\mathrm{d}u}{\mathrm{d}t} = L(u), \tag{19}$$

the general m-stage low-storage Runge-Kutta scheme [5, 36] can be written in the form

$$\begin{aligned} &u^{(0)} = u^n, && v^{(0)} = 0, \\ &v^{(i)} = a_i v^{(i-1)} + \Delta t L(u^{(i-1)}), && i = 1, \ldots, m, \\ &u^{(i)} = u^{(i-1)} + b_i v^{(i)}, && i = 1, \ldots, m, \\ &u^{n+1} = u^{(m)}, \end{aligned} \tag{20}$$

where only u and an auxiliary variable v must be stored. The coefficients a_i and b_i have been determined for a number of different low-storage Runge-Kutta schemes. See [5] and [13] for

Table 1 Coefficients of the fourth-order five-stage low-storage Runge-Kutta method

i	a_i	b_i
1	0	0.14965902199923
2	−0.41789047449985	0.37921031299963
3	−1.19215169464268	0.82295502938698
4	−1.69778469247153	0.69945045594912
5	−1.51418344425716	0.15305724796815

more details. In this article we consider the fourth-order five-stage low-storage scheme also applied in [18]. The coefficients we use are listed in Table 1.

One possible way to achieve a weaker time-step restriction is the application of SSP-RK schemes. In [14] it was shown that for the linear autonomous system (19) the class of m-stage linear SSP-RK schemes, given recursively by

$$\begin{aligned} u^{(0)} &= u^n, \\ u^{(i)} &= u^{(i-1)} + \Delta t L u^{(i-1)}, \quad i = 1, \ldots, m-1, \\ u^{(m)} &= \sum_{k=0}^{m-2} \alpha_{m,k} u^{(k)} + \alpha_{m,m-1}(u^{(m-1)} + \Delta t L u^{(m-1)}), \\ u^{n+1} &= u^{(m)}, \end{aligned} \tag{21}$$

where $\alpha_{1,0} = 1$ and

$$\alpha_{m,k} = \frac{1}{k}\alpha_{m-1,k-1}, \quad k = 1, \ldots, m-2,$$

$$\alpha_{m,m-1} = \frac{1}{m!}, \qquad \alpha_{m,0} = 1 - \sum_{k=1}^{m-1} \alpha_{m,k},$$

are mth-order accurate. This was extended to linear non-autonomous systems by Chen et al. [6]. In that work the authors demonstrated that when applied together with the classical discontinuous Galerkin method [9, 11], the SSP-RK scheme gives $(p+1)$st-order convergence with the stability bound

$$\mathrm{CFL}(p) = \mathrm{C}\frac{1}{2p+1} \tag{22}$$

with $\mathrm{C} = 1$, as long as for a given spatial discretisation of polynomial order p, the corresponding SSP-RK method has order $p+1$. The stability regions of several SSP-RK methods and the low-storage five-stage fourth-order Runge-Kutta method are displayed in Fig. 2.

5 Analysis of the Dispersion and Dissipation Error

A critical factor in the numerical simulation of wave-propagation is the artificial dissipation and/or dispersion inflicted on the waves due to numerical discretisation errors. In order to analyse these properties of the different schemes, we resort to the one-dimensional and two-dimensional forms of the Maxwell equations with periodic boundary conditions. First, these

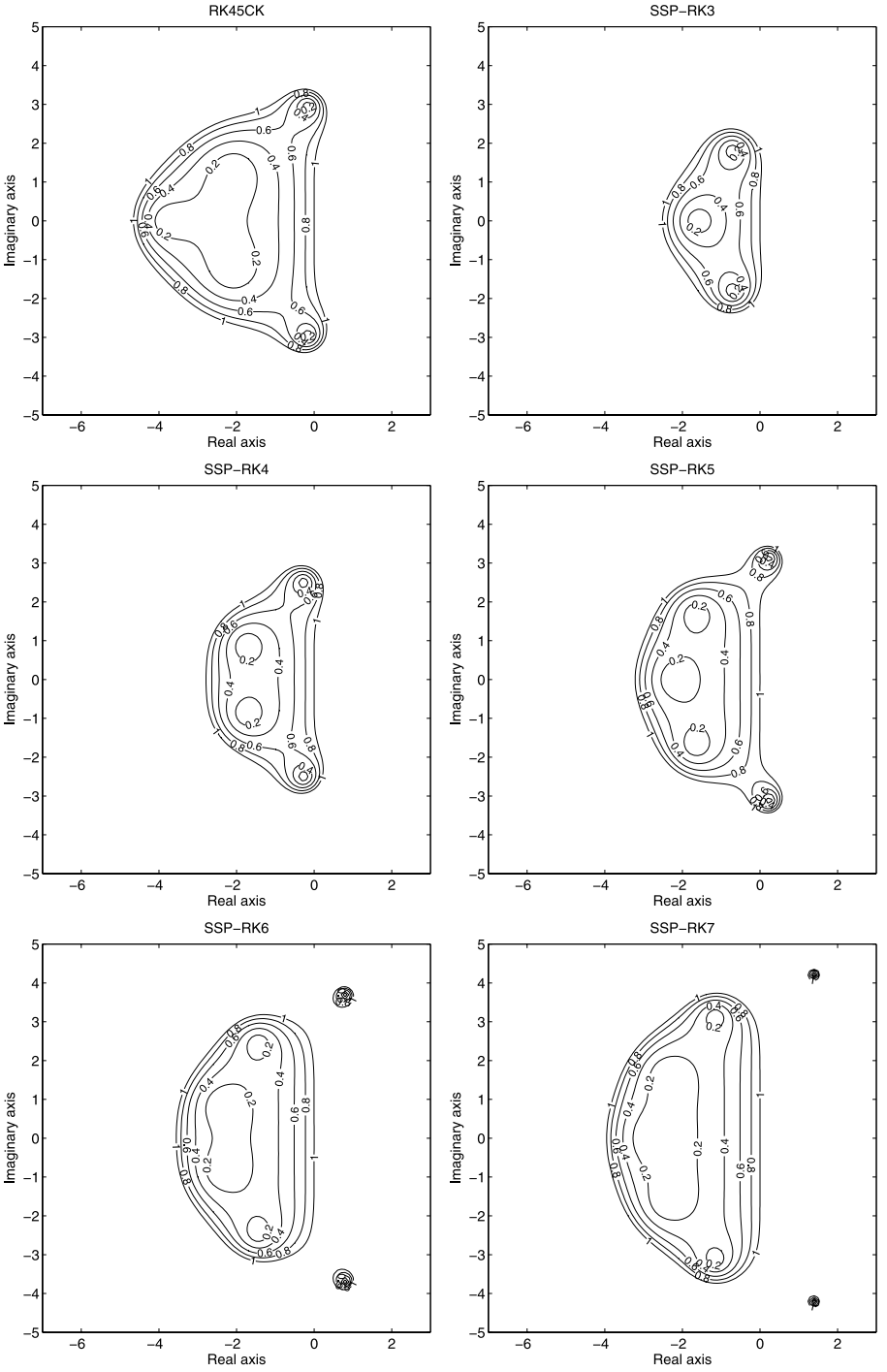

Fig. 2 Stability regions for the five-stage fourth-order Runge-Kutta method (*top left*) and for five different SSP-RK methods of order $m = 3, 4, 5, 6, 7$

reduced models are formulated and then we perform a numerical Fourier analysis of the fully discrete schemes to investigate the dispersion and dissipation errors as a function of mesh size per wave length and time step. This analysis provides important information on the accuracy of the schemes regarding wave motion and the relation between time step, mesh size and polynomial order.

5.1 Wave Equation in One and Two Dimensions

The Maxwell equations in one dimension read

$$\varepsilon_{\mathrm{r}}\frac{\partial E}{\partial t}=-\frac{\partial H}{\partial x},\qquad \mu_{\mathrm{r}}\frac{\partial H}{\partial t}=-\frac{\partial E}{\partial x}, \tag{23}$$

or they can be expressed by the wave equation

$$\frac{\partial^2 E}{\partial t^2}-\frac{1}{\varepsilon_{\mathrm{r}}\mu_{\mathrm{r}}}\frac{\partial^2 E}{\partial x^2}=0,$$

in the domain $\Omega\subset\mathbb{R}$. In conservative form (7), this reads

$$Q\frac{\partial \boldsymbol{q}}{\partial t}+\nabla\cdot\boldsymbol{F}(\boldsymbol{q})=0 \tag{24}$$

with

$$Q=\mathtt{diag}(\varepsilon_{\mathrm{r}},\mu_{\mathrm{r}}),\qquad \boldsymbol{q}=\begin{bmatrix}E\\H\end{bmatrix},\qquad \boldsymbol{F}(\boldsymbol{q})=\begin{bmatrix}H\\E\end{bmatrix}.$$

For the two-dimensional analysis we take the transverse magnetic (TM) polarisation of the Maxwell equations

$$\begin{aligned}\mu_{\mathrm{r}}\frac{\partial H^x}{\partial t}&=-\frac{\partial E^z}{\partial y},\\ \mu_{\mathrm{r}}\frac{\partial H^y}{\partial t}&=\frac{\partial E^z}{\partial x},\\ \varepsilon_{\mathrm{r}}\frac{\partial E^z}{\partial t}&=\frac{\partial H^y}{\partial x}-\frac{\partial H^x}{\partial y},\end{aligned}$$

which is again equivalent to the second-order wave equation,

$$\frac{\partial^2 E^z}{\partial t^2}-\frac{1}{\varepsilon_{\mathrm{r}}\mu_{\mathrm{r}}}\nabla^2 E^z=0.$$

Thus we arrive at the first-order system (7)

$$Q\frac{\partial \boldsymbol{q}}{\partial t}+\nabla\cdot\boldsymbol{F}(\boldsymbol{q})=0, \tag{25}$$

with

$$Q=\mathtt{diag}(\mu_{\mathrm{r}},\mu_{\mathrm{r}},\varepsilon_{\mathrm{r}}),\qquad \boldsymbol{q}=\begin{bmatrix}H^x\\H^y\\E^z\end{bmatrix},\qquad \boldsymbol{F}(\boldsymbol{q})=\begin{bmatrix}0 & -E^z\\ E^z & 0\\ H^y & -H^x\end{bmatrix}.$$

5.2 Dispersion and Dissipation Analysis of the Global Scheme

For the analysis of the fully discrete schemes, we consider (24) and (25) in the domains $\Omega = [-1, 1]$ and $\Omega = [-1, 1]^2$, respectively. Furthermore, we use uniform meshes and assume that the boundaries are periodic.

5.2.1 One-Dimensional Fourier Analysis

We are primarily interested in wave propagation and in the associated dispersion and dissipation error of the RKDG scheme. We consider the one-dimensional semi-discrete scheme (16)

$$\frac{\mathrm{d}\boldsymbol{q}_h}{\mathrm{d}t} = \boldsymbol{\mathcal{A}}\boldsymbol{q}_h$$

in the domain $\Omega = [-1, 1]$ filled with vacuum (or air) and assume a monochromatic plane wave (which is also a Fourier mode)

$$\boldsymbol{q}_h(0) = \boldsymbol{q}_h^0 = [\mathrm{e}^{\mathrm{i}kx_h}, \mathrm{e}^{\mathrm{i}kx_h}]^T$$

as initial condition. Here, x_h represents the vector of the nodes used for the spatial discretisation. We denote the angular wave frequency with ω. The exact wave number k is given by the dispersion relation $k^2 = \omega^2/c^2$, with c being the speed of light. The time-exact discrete Fourier mode at time level $t_n = n\Delta t$ will read

$$\boldsymbol{q}_h(n\Delta t) = \nu^n \boldsymbol{q}_h(0) = \mathrm{e}^{-\mathrm{i}\omega n\Delta t}[\mathrm{e}^{\mathrm{i}kx_h},\ \mathrm{e}^{\mathrm{i}kx_h}]^T \tag{26}$$

with exact amplification factor $\nu^n = \mathrm{e}^{-\mathrm{i}\omega n\Delta t}$ and $\mathrm{i}^2 = -1$. To see the effect of the time-stepping method, we replace the exact amplification factor ν^n with its discrete counterpart ν_h^n and take the fully discrete Fourier mode as

$$\boldsymbol{q}_h^n = \nu_h^n \boldsymbol{q}_h^0 = \nu_h^n[\mathrm{e}^{\mathrm{i}kx_h}, \mathrm{e}^{\mathrm{i}kx_h}]^T. \tag{27}$$

In addition, we write the SSP-RK scheme as a two-level explicit scheme. Thus

$$\boldsymbol{q}_h^{n+1} = \boldsymbol{\mathcal{B}}\boldsymbol{q}_h^n \tag{28}$$

holds with amplification matrix

$$\boldsymbol{\mathcal{B}} = \sum_{l=0}^{m} \frac{1}{l!}(\Delta t\boldsymbol{\mathcal{A}})^l \tag{29}$$

and with m being the order of the SSP-RK time-stepping scheme. Substituting (27) into (28) results in the equation

$$\nu_h^{n+1}[\mathrm{e}^{\mathrm{i}kx_h},\ \mathrm{e}^{\mathrm{i}kx_h}]^T = \boldsymbol{\mathcal{B}}\nu_h^n[\mathrm{e}^{\mathrm{i}kx_h}, \mathrm{e}^{\mathrm{i}kx_h}]^T,$$

which, after division with ν_h^n, reduce to the eigenvalue problem

$$\nu_h\boldsymbol{q}_h^0 = \boldsymbol{\mathcal{B}}\boldsymbol{q}_h^0. \tag{30}$$

Solving this eigenvalue equation will produce $p+1$ different values for $\nu_{h,j}$ (and as many corresponding eigenvectors $\boldsymbol{q}^0_{h,j}$). Bearing in mind that

$$\nu_{h,j} = \mathrm{e}^{-\mathrm{i}\tilde{\omega}_{h,j}\Delta t},$$

with *complex* numerical frequencies $\tilde{\omega}_{h,j}$, we can establish the dispersion and dissipation properties of the scheme. For that, we consider the real (for dispersion) and imaginary (for dissipation) parts of the complex numerical frequencies $\tilde{\omega}_{h,j} = (\mathrm{i}/\Delta t)\ln \nu_{h,j}$, that is

$$\omega_{h,j} = \mathrm{Re}[\tilde{\omega}_{h,j}] = \mathrm{Re}[(\mathrm{i}/\Delta t)\ln \nu_{h,j}], \qquad \rho_{h,j} = \mathrm{Im}[\tilde{\omega}_{h,j}] = \mathrm{Im}[(\mathrm{i}/\Delta t)\ln \nu_{h,j}],$$

with *real* numerical frequency $\omega_{h,j}$ and numerical dissipation $\rho_{h,j}$, both corresponding to the eigenvalue $\nu_{h,j}$. One of the computed modes will be close to the frequency of the physical mode. This represents the approximation properties of our scheme. The other modes are spurious. To decide which eigenvalue should be considered, we define the dissipation error as $\mathrm{err}^{\mathrm{diss}}_{h,j} = |\rho_{h,j}| - 1$ and the dispersion error as the absolute value of dispersion error $\mathrm{err}^{\mathrm{disp}}_{h,j} = |\omega - \omega_{h,j}|$. The numerical Fourier mode is now taken as the closest eigenvalue to the physical mode

$$\nu_h := \left\{ \nu_{h,j} : \min_j \sqrt{(\mathrm{err}^{\mathrm{disp}}_{h,j})^2 + (\mathrm{err}^{\mathrm{diss}}_{h,j})^2} \right\}. \tag{31}$$

In the numerical dispersion and dissipation analysis of the fully discrete schemes, we consider a wide range of values for Δt and h_k. The eigenvalues of (30) are computed in `Matlab`.

It is also important to consider the convergence of the numerical dispersion and dissipation error. In [1] a complete dispersion and dissipation analysis of the semi-discrete advection equation was carried out for discontinuous Galerkin methods with high-order tensor-product elements. In that article it was proven that in the asymptotic region $hk = \frac{2\pi h}{\lambda} \to 0$ (with λ being the wave length) the dispersion relation for a pth-order method is accurate to order $2p+3$ for the dispersion error and order $2p+2$ for the dissipation error. See [22] and [1] for more details. In a more recent work [2] the dispersion and dissipation analysis of the semi-discrete wave equation was provided for some low-order schemes (linear elements for the general DG and up to third order elements for the IP-DG) and the authors also conjectured on how the results would extend to arbitrary order elements. For the fully discrete system we consider here, the rate of convergence is also influenced by the time-stepping method. However, for most polynomial orders p, the convergence of the dispersion and dissipation error still by far supersedes that of the error measured in the l^2-norm. The numerical results are discussed in Sect. 6.

5.2.2 *Two-Dimensional Fourier Analysis*

As in one dimension, we assemble our right-hand side into a global matrix and consider the abstract Cauchy problem (16)

$$\frac{\mathrm{d}\boldsymbol{q}_h}{\mathrm{d}t} = \boldsymbol{\mathcal{A}}\boldsymbol{q}_h,$$

where now $\boldsymbol{q} = [H^x_h, H^y_h, E^z_h]^T$ and the matrix $\boldsymbol{\mathcal{A}}$ represents the semi-discrete system resulting from the discretisation of (25). The only difference in the mathematical formulation

Table 2 Convergence of the global error for the one-dimensional metallic cavity filled with two different materials. In each case the $(p+1)$st-order SSP-RK scheme is applied

	$p=1$		$p=2$		$p=3$	
	l^2-error	Order	l^2-error	Order	l^2-error	Order
$N_{\mathrm{el}}=2$	1.7557E-00		2.5843e+00		1.3544E-00	
$N_{\mathrm{el}}=4$	1.5732E-00	1.5840	7.9723E-01	1.6967	2.0100E-01	2.7524
$N_{\mathrm{el}}=8$	8.4106E-01	9.0339	1.0048E-01	2.9880	1.7313E-02	3.5372
$N_{\mathrm{el}}=16$	1.9518E-01	2.1074	1.4226E-02	2.8204	1.1295E-03	3.9382
$N_{\mathrm{el}}=32$	3.8904E-02	2.3268	1.8855E-03	2.9155	6.8300E-05	4.0476
$N_{\mathrm{el}}=64$	9.0807E-03	2.0990	2.3897E-04	2.9800	4.3243E-06	3.9813
$N_{\mathrm{el}}=128$	2.2310E-03	2.0251	2.9985E-05	2.9945	2.7049E-07	3.9988
$N_{\mathrm{el}}=256$	5.5755E-04	2.0005	3.7547E-06	2.9975	1.6909E-08	3.9997
$N_{\mathrm{el}}=512$	1.3944E-04	1.9995	4.6972E-07	2.9988	1.0568E-09	4.0000
	$p=4$		$p=5$		$p=6$	
	l^2-error	Order	l^2-error	Order	l^2-error	Order
$N_{\mathrm{el}}=2$	7.7746E-01		2.7975E-01		1.6624E-01	
$N_{\mathrm{el}}=4$	5.7034E-02	3.7689	1.0551E-02	4.7286	1.8202E-03	6.5130
$N_{\mathrm{el}}=8$	1.9711E-03	4.8548	2.0173E-04	5.7089	1.6440E-05	6.7907
$N_{\mathrm{el}}=16$	6.5391E-05	4.9138	3.1504E-06	6.0007	1.3514E-07	6.9267
$N_{\mathrm{el}}=32$	2.0736E-06	4.9789	4.9661E-08	5.9873	1.0574E-09	6.9978
$N_{\mathrm{el}}=64$	6.4733E-08	5.0015	7.7594E-10	6.0000	8.3515E-12	6.9843
$N_{\mathrm{el}}=128$	1.9895E-09	5.0240	1.2161E-11	5.9956		
$N_{\mathrm{el}}=256$	6.2218E-11	4.9989	2.7547E-13	5.4642		
	$p=7$		$p=8$		$p=9$	
	l^2-error	Order	l^2-error	Order	l^2-error	Order
$N_{\mathrm{el}}=2$	1.4124E-02		1.5533E-02		7.3602E-04	
$N_{\mathrm{el}}=4$	2.7117E-04	5.7028	3.7314E-05	8.7014	4.4752E-06	7.3616
$N_{\mathrm{el}}=8$	1.2568E-06	7.7533	8.2859E-08	8.8149	4.9118E-09	9.8315
$N_{\mathrm{el}}=16$	5.0129E-09	7.9699	1.6508E-10	8.9714	4.9240E-12	9.9622
$N_{\mathrm{el}}=32$	1.9730E-11	7.9891	3.2760E-13	8.9770		

to the one-dimensional case is that the dispersion relation now reads $k_x^2+k_y^2=\omega^2/c^2$. The time-exact discrete Fourier mode satisfying (25) is equal to

$$\boldsymbol{q}_h^n = \nu^n[(k_y/\omega)\mathrm{e}^{\mathrm{i}k_x x_h+\mathrm{i}k_y y_h}, (-k_x/\omega)\mathrm{e}^{\mathrm{i}k_x x_h+\mathrm{i}k_y y_h}, \mathrm{e}^{\mathrm{i}k_x x_h+\mathrm{i}k_y y_h}]^T \tag{32}$$

in the two-dimensional domain $\Omega=[-1,1]^2$. From here we follow exactly the same line as in the one-dimensional case. As initial condition we take a monochromatic plane wave with different wave numbers k_y and k_x between which the relation $k_y=2k_x$ always holds. This represents a monochromatic plane wave travelling at an angle of about 26.565° against the x axis. As in one dimension, a range of values of Δt and h_k are considered. We note that for computing the matrix exponential in (29) the simple Horner's rule is applied (see [12] for example).

Table 3 Errors and computational work when different time-stepping schemes are applied to the cavity problem with polynomial order p, number of elements N_{el} and degrees of freedom DoF after integrating over $T = 1000$ time periods

$p = 3$, $N_{\text{el}} = 40$ (DoF = 160)	$\Delta t = \Delta t_{\max}$	ops	l^∞-error	l^2-error
SSP-RK4	7.1428E-03	560004	4.2370E-04	2.1220E-04
Carpenter&Kennedy	5.5555E-03	900005	6.2719E-05	3.1442E-05
Standard RK4	5.5555E-03	720004	1.5559E-04	7.7676E-05
$p = 3$, $N_{\text{el}} = 20$ (DoF = 80)	$\Delta t = \Delta t_{\max}$	ops	l^∞-error	l^2-error
SSP-RK4	1.4286E-02	280004	6.6828E-03	3.3938E-03
Carpenter&Kennedy	1.1111E-02	450005	9.5898E-04	5.2903E-04
Standard RK4	1.1111E-02	360004	2.4328E-03	1.2492E-03
$p = 6$, $N_{\text{el}} = 12$ (DoF = 84)	$\Delta t = \Delta t_{\max}$	ops	l^∞-error	l^2-error
SSP-RK7	1.2820E-02	546007	1.5364E-07	6.4372E-08
Carpenter&Kennedy	9.2592E-03	540005	4.7966E-04	2.3993E-04
Standard RK4	9.2592E-03	432004	1.1982E-03	5.9976E-04
$p = 6$, $N_{\text{el}} = 6$ (DoF = 42)	$\Delta t = \Delta t_{\max}$	ops	l^∞-error	l^2-error
SSP-RK7	2.5640E-02	273007	1.7646E-05	8.0618E-06
Carpenter&Kennedy	1.8518E-02	270005	7.6505E-03	3.8385E-03
Standard RK4	1.8518E-02	216004	1.9066E-02	9.5896E-03
$p = 10$, $N_{\text{el}} = 4$ (DoF = 44)	$\Delta t = \Delta t_{\max}$	ops	l^∞-error	l^2-error
SSP-RK11	2.3810E-02	462000	1.9624E-08	9.7129E-09
Carpenter&Kennedy	1.0000E-02	500000	6.5246E-04	2.6565E-04
Standard RK4	1.0000E-02	400000	1.6297E-03	6.6450E-04
$p = 10$, $N_{\text{el}} = 2$ (DoF = 22)	$\Delta t = \Delta t_{\max}$	ops	l^∞-error	l^2-error
SSP-RK11	4.7619E-02	231000	3.3137E-06	3.2341E-06
Carpenter&Kennedy	2.0000E-02	250000	1.0199E-02	4.5032E-03
Standard RK4	2.0000E-02	200000	2.5387E-02	1.1272E-02

6 Numerical Results

6.1 One-Dimensional Cavity

In order to investigate if the SSP-RK scheme retains the high-order convergence of the spatial discretisation [18], we consider the one-dimensional cavity problem in the domain $x \in [-1, 1]$, with two different non-magnetic ($\mu_{\text{r},1} = \mu_{\text{r},2} = 1$) materials. The material interface is situated at $x = 0$ and the two different materials have a relative permittivity of $\varepsilon_{\text{r},1} = 1$ and $\varepsilon_{\text{r},2} = 2.25$, respectively. The error is measured against the exact solution, which is included in the Appendix. We set the frequency of the wave at $\omega = 2\pi$, the same throughout the whole domain, which entails the corresponding wave numbers $k_1 = 2\pi$ and $k_2 = 3\pi$, respectively. In Table 2 we show the l_2-error $\|\boldsymbol{q}_N - \boldsymbol{q}_{\text{exact}}\|$ at final time $T = 1$ for different orders of the local polynomials. For the time integration, we use the $(p+1)$st-order SSP-RK

Table 4 Computational work needed to achieve at least $l^2_{\text{err}} = 10^{-5}$ accuracy when different time-stepping schemes are applied to the cavity problem with polynomial order p, number of elements N_{el} and degrees of freedom DoF after integrating over $T = 1000$ time periods

$p = 3$, $N_{\text{el}} = 54$ (DoF = 216)	Δt	ops	l^2-error
SSP-RK4	3.2922E-03	1215004	9.7349E-06
Carpenter&Kennedy	4.1152E-03	1215005	9.4976E-06
Standard RK4	3.2922E-03	1215004	9.7349E-06
$p = 6$, $N_{\text{el}} = 6$ (DoF = 42)	Δt	ops	l^2-error
SSP-RK7	2.5640E-02	273007	8.0618E-06
Carpenter&Kennedy	3.7037E-03	1350005	9.5547E-06
Standard RK4	2.7778E-03	1440004	8.9196E-06
$p = 10$, $N_{\text{el}} = 2$ (DoF = 22)	Δt	ops	l^2-error
SSP-RK11	4.7619E-02	231000	3.2341E-06
Carpenter&Kennedy	4.0000E-03	1250000	7.7825E-06
Standard RK4	3.0000E-03	1333336	6.4107E-06

method (21) with corresponding maximum time step (22). We can see that in the asymptotic region $hk \ll 1$, $(p+1)$st-order convergence is achieved for polynomial orders p in the range of $1 \leq p \leq 9$.

In the next example we compare the performance of the two different time-integration schemes defined in Sect. 4. We also include the ubiquitous standard fourth-order RK scheme as a reference. The constant in the time-step restriction (22) of the SSP-RK schemes is set to $\mathrm{C} = 1$ for all values of polynomial order p. For the low-storage Runge-Kutta scheme and the standard Runge-Kutta scheme, we use the value $\mathrm{C} = 1$ in (18) for $p \leq 5$, and the value $\mathrm{C} = 2$ when $5 < p \leq 10$. We consider the same cavity, but now filled with vacuum (or air) and integrate for a relatively long time, until $T = 1000$ time periods. The results are shown in Table 3 for different orders and different number of elements. We measure the computational work as the number of operations, which is simply computed as

$$\mathtt{ops} = N_{\mathrm{T}} m,$$

where N_T is the number of time steps needed until final time T, and m represents the number of stages in a given RK scheme. For each RK scheme we use the corresponding maximum time step defined in Sect. 4. The test was carried out for orders $p = 3$, $p = 6$ and $p = 10$. Significant differences in accuracy, up to $\mathcal{O}(4)$, occur between the schemes for orders $p = 6$ and $p = 10$. For each order, we include two subtables, one for a relatively fine spatial grid and one for a comparatively coarse one. The most favourable characteristic of the SSP-RK schemes is that the better accuracy occurs without significant—or indeed, any—increase in the number of operations.

Perhaps even more illuminating is to see how much computational work is needed to obtain a given accuracy. In Table 4 we show the number of operations necessary to achieve the error $l^2_{\text{err}} = 10^{-5}$ at final time $T = 1000$. The comparisons of the different time-integration schemes are made for fixed polynomial order and spatial mesh, so that only the time step was lowered in order to decrease the errors.

Table 5 Convergence of the dispersion error for the one-dimensional wave equation in a periodic domain with wave numbers $k = \pi$ for $p = 1, 2$; $k = 2\pi$ for $p = 3, 4$; $k = 4\pi$ for $p = 5, 6, 7$; and $k = 8\pi$ for $p = 8, 9, 10$. In each case the $(p + 1)$st-order SSP-RK scheme is applied

	$p = 1$		$p = 2$			
	Error	Order	Error	Order		
$N_{el} = 2$	1.1219E-00		5.4535E-02			
$N_{el} = 4$	1.8866E-01	2.5721	1.9858E-03	4.7794		
$N_{el} = 8$	3.9271E-02	2.2642	8.0576E-05	4.6232		
$N_{el} = 16$	9.1970E-03	2.0942	4.2539E-06	4.2435		
$N_{el} = 32$	2.2573E-03	2.0266	2.5327E-07	4.0700		
$N_{el} = 64$	5.6163E-04	2.0069	1.5631E-08	4.0182		
	$p = 3$		$p = 4$			
	Error	Order	Error	Order		
$N_{el} = 2$	2.8401E-01		4.3239E-02			
$N_{el} = 4$	1.8427E-03	7.2680	8.7429E-05	8.9500		
$N_{el} = 8$	1.1103E-04	4.0528	9.1380E-08	9.9020		
$N_{el} = 16$	8.1803E-06	3.7626	3.1783E-09	4.8456		
$N_{el} = 32$	5.1772E-07	3.9819	5.1479E-11	5.9481		
$N_{el} = 64$	3.2403E-08	3.9980	8.0824E-13	5.9930		
	$p = 5$		$p = 6$		$p = 7$	
	Error	Order	Error	Order	Error	Order
$N_{el} = 2$	2.2250E-00		6.2763E-01		1.4307E-01	
$N_{el} = 4$	7.5731E-03	8.1987	4.3307E-04	10.501	1.8263E-05	12.936
$N_{el} = 8$	4.8796E-06	10.600	4.9182E-08	13.104	3.2505E-10	15.778
$N_{el} = 16$	2.1995E-08	7.7934	1.5744E-11	11.609	4.6185E-13	9.4590
$N_{el} = 32$	3.2993E-10	6.0589				
$N_{el} = 64$	5.1621E-12	5.9981				
	$p = 8$		$p = 9$		$p = 10$	
	Error	Order	Error	Order	Error	Order
$N_{el} = 2$	3.8264E-00		8.3880E-01		1.5821E-00	
$N_{el} = 4$	4.9854E-02	6.2621	6.5271E-03	7.0057	6.6177E-04	11.223
$N_{el} = 8$	1.1951E-06	15.348	3.1177E-08	17.676	6.6458E-10	19.925
$N_{el} = 16$	6.6187E-12	17.462				

6.2 Numerical Dispersion and Dissipation Error

To conduct the dispersion and dissipation analysis described in Sect. 5, we carry out two types of experiments. First, we consider the convergence of the dispersion and dissipation errors in one dimension. The polynomials we apply for the spatial discretisation range from $p = 1$ to $p = 10$, and for the time discretisation we use the corresponding $(p + 1)$st-order SSP-RK scheme (21) with maximum time step (22). Because the actual errors may be rather small for large values of p, we increase the wave number (thus decrease the wave length) for higher-order polynomials. Consequently, the following wave numbers are used in our

Table 6 Convergence of the dissipation error for the one-dimensional wave equation in a periodic domain with wave numbers $k = \pi$ for $p = 1, 2$; $k = 2\pi$ for $p = 3, 4$; $k = 4\pi$ for $p = 5, 6, 7$; and $k = 8\pi$ for $p = 8, 9, 10$. In each case the $(p + 1)$st-order SSP-RK scheme is applied

	$p = 1$		$p = 2$			
	Error	Order	Error	Order		
$N_{\mathrm{el}} = 2$	2.5464E-01		2.1860E-02			
$N_{\mathrm{el}} = 4$	1.6710E-02	3.9297	7.5294E-04	4.8596		
$N_{\mathrm{el}} = 8$	1.1239E-03	3.8941	3.1441E-05	4.5818		
$N_{\mathrm{el}} = 16$	7.2499E-05	3.9544	1.6831E-06	4.2235		
$N_{\mathrm{el}} = 32$	4.5729E-06	3.9868	1.0063E-07	4.0640		
$N_{\mathrm{el}} = 64$	2.8649E-07	3.9966	6.2172E-09	4.0166		
	$p = 3$		$p = 4$			
	Error	Order	Error	Order		
$N_{\mathrm{el}} = 2$	6.1234E-02		6.2971E-03			
$N_{\mathrm{el}} = 4$	6.8779E-04	6.4762	1.4252E-05	8.7873		
$N_{\mathrm{el}} = 8$	4.2695E-06	7.3318	1.8226E-08	9.6110		
$N_{\mathrm{el}} = 16$	2.8124E-08	7.2461	5.9037E-10	4.9482		
$N_{\mathrm{el}} = 32$	2.7328E-10	6.6852	9.5566E-12	5.9490		
$N_{\mathrm{el}} = 64$	3.6039E-12	6.2447	1.5099E-13	5.9840		
	$p = 5$		$p = 6$		$p = 7$	
	Error	Order	Error	Order	Error	Order
$N_{\mathrm{el}} = 2$	1.7209E-01		3.8318E-02		8.3102E-03	
$N_{\mathrm{el}} = 4$	5.4651E-04	8.2987	3.2754E-05	10.192	1.4167E-06	12.518
$N_{\mathrm{el}} = 8$	2.8854E-07	10.887	4.0972E-09	12.965	3.7758E-11	15.195
$N_{\mathrm{el}} = 16$	5.7239E-11	12.300	1.3922E-12	11.523		
	$p = 8$		$p = 9$		$p = 10$	
	Error	Order	Error	Order	Error	Order
$N_{\mathrm{el}} = 2$	8.7179E-02		1.1417E-01		4.0277E-02	
$N_{\mathrm{el}} = 4$	1.5076E-03	5.8536	2.0997E-04	9.0867	2.2413E-05	10.811
$N_{\mathrm{el}} = 8$	4.6922E-08	14.972	1.2343E-09	17.376	2.6468E-11	19.692
$N_{\mathrm{el}} = 16$	2.7467E-13	17.382				

one-dimensional Fourier analysis:

$$k = \begin{cases} \pi & \text{if } p = 1, 2, \\ 2\pi & \text{if } p = 3, 4, \\ 4\pi & \text{if } p = 5, 6, 7, \\ 8\pi & \text{if } p = 8, 9, 10. \end{cases}$$

The errors, defined in Sect. 5, and the rate of the convergence are shown in Table 5 for the dispersion and in Table 6 for the dissipation. Although we cannot establish precise convergence rates due the influence of the time discretisation on the dispersion and dissipation properties, an order of convergence of approximately $2p$ is achieved for both the dissipation

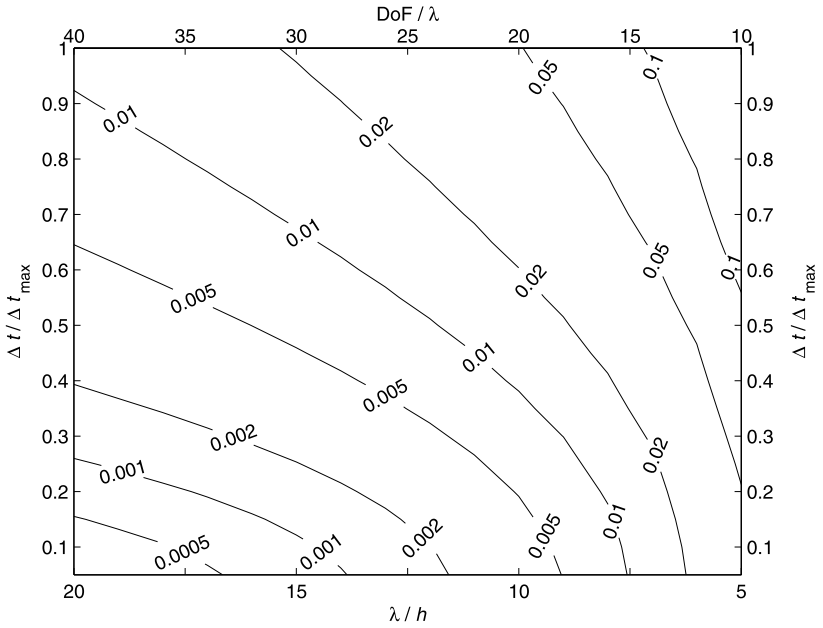

(a) $p = 1$

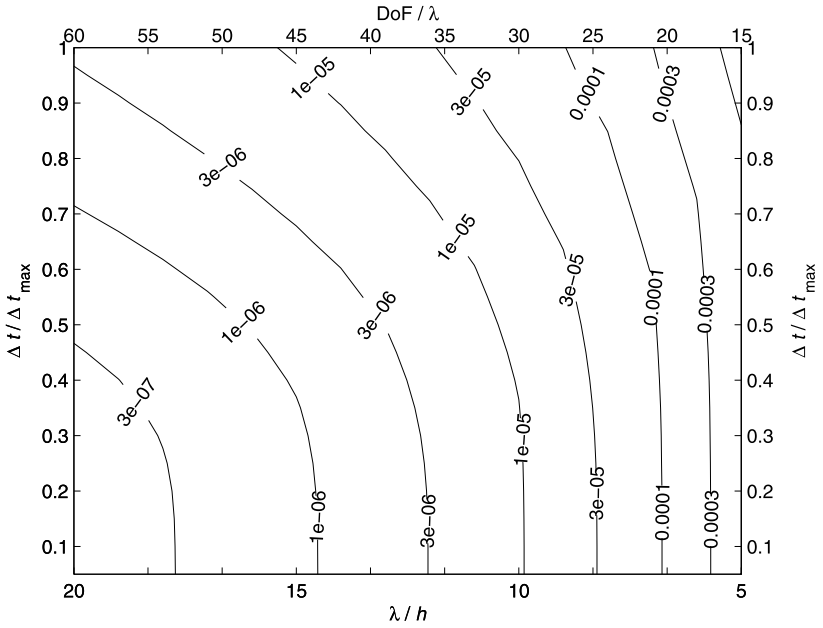

(b) $p = 2$

Fig. 3 Absolute value of the dispersion error as a function of wave length per mesh size (λ/h), degrees of freedom per wavelength (DoF/λ) and relative time step ($\Delta t/\Delta t_{\max}$) for polynomial orders $p = 1, 2$

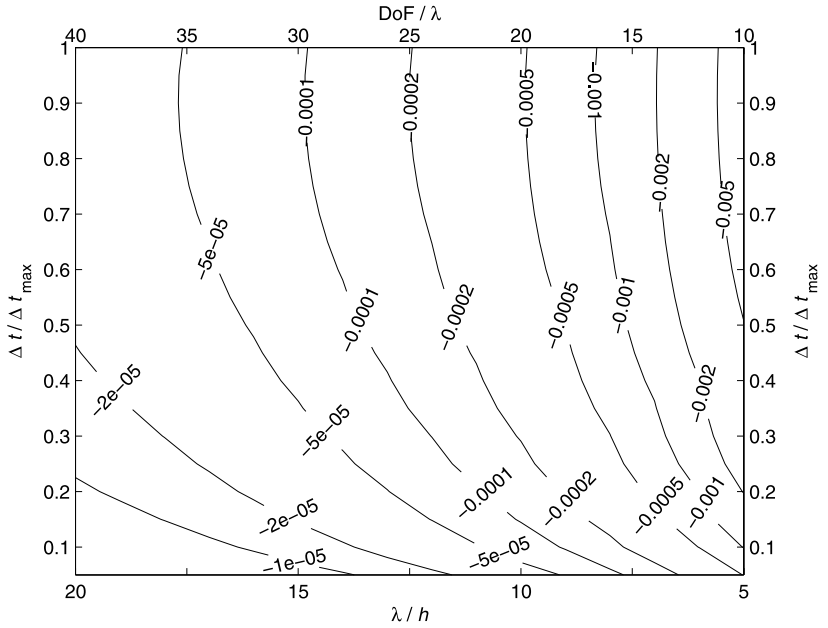

(a) $p = 1$

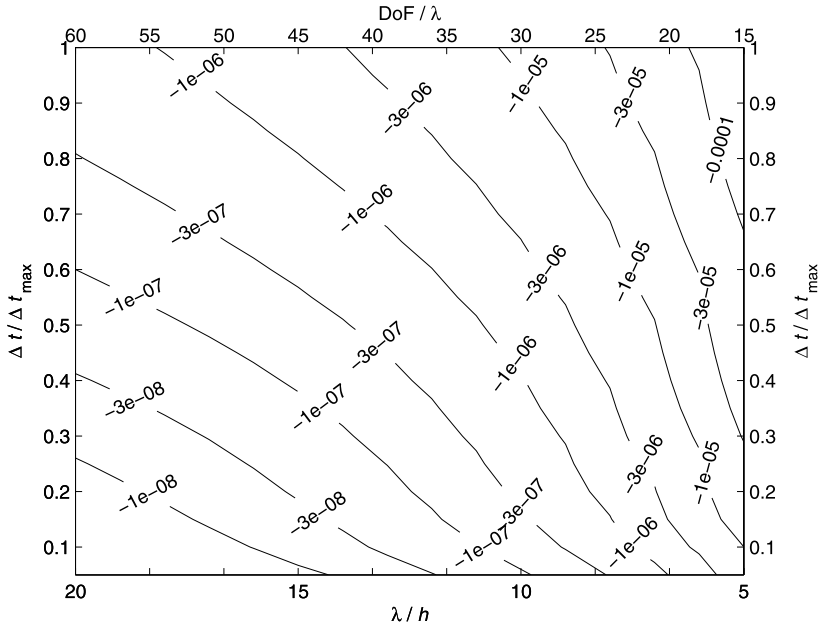

(b) $p = 2$

Fig. 4 Dissipation error as a function of wave length per mesh size (λ/h), degrees of freedom per wavelength (DoF/λ) and relative time step ($\Delta t/\Delta t_{\max}$) for polynomial orders $p = 1, 2$

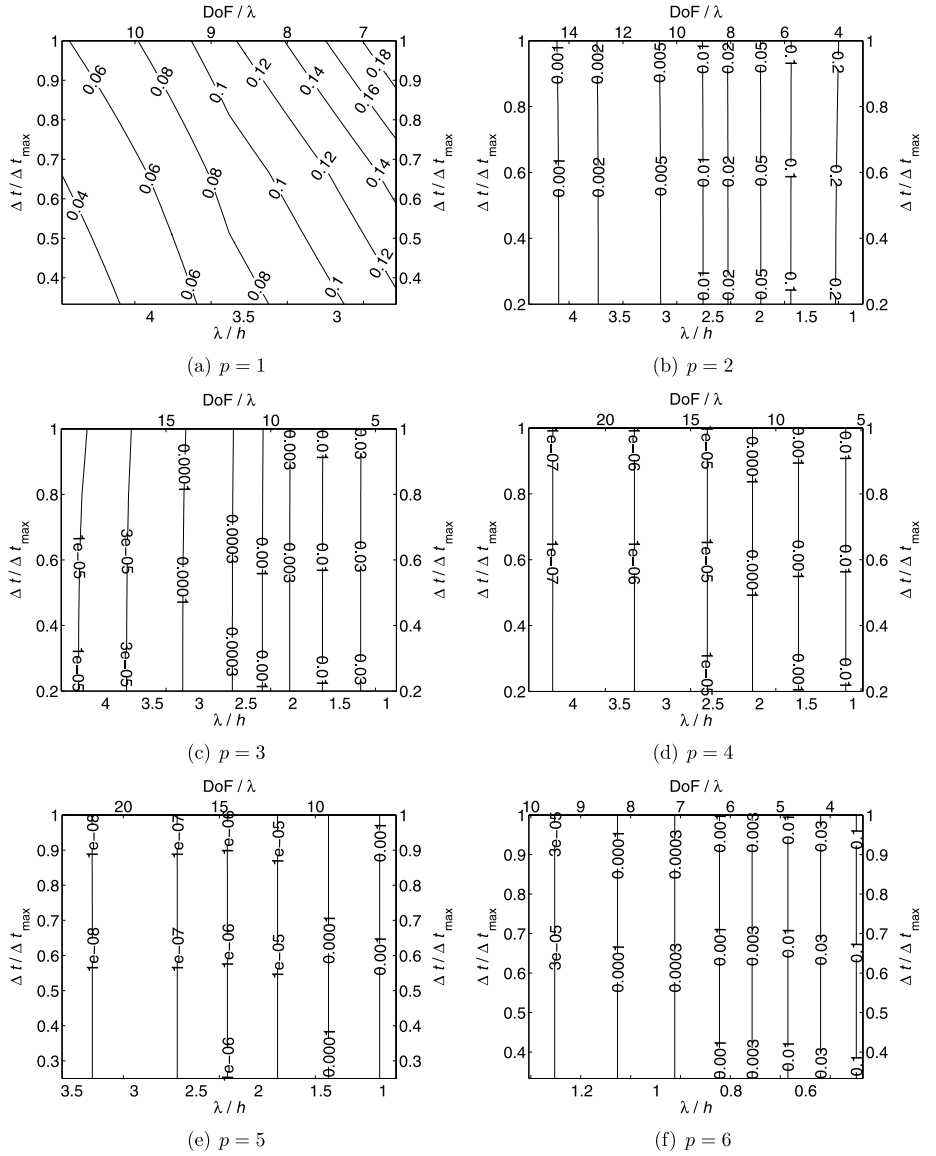

Fig. 5 Absolute value the of dispersion error as a function of wave length per mesh size (λ/h), degrees of freedom per wavelength (DoF/λ) and relative time step ($\Delta t/\Delta t_{\max}$) for polynomial orders $p = 1, 2, 3, 4, 5, 6$ on a uniform mesh

and dispersion error. Comparing these results to the findings of [1] and [2] already implies that the SSP-RK time integration has a less dominant effect on the dispersion and dissipation errors.

In the second experiment, we consider a wide range of time steps Δt and mesh sizes h, and examine the dispersion and dissipation errors of the schemes as a function of wave length per mesh size (λ/h), degrees of freedom per wave length (DoF/λ) and relative time

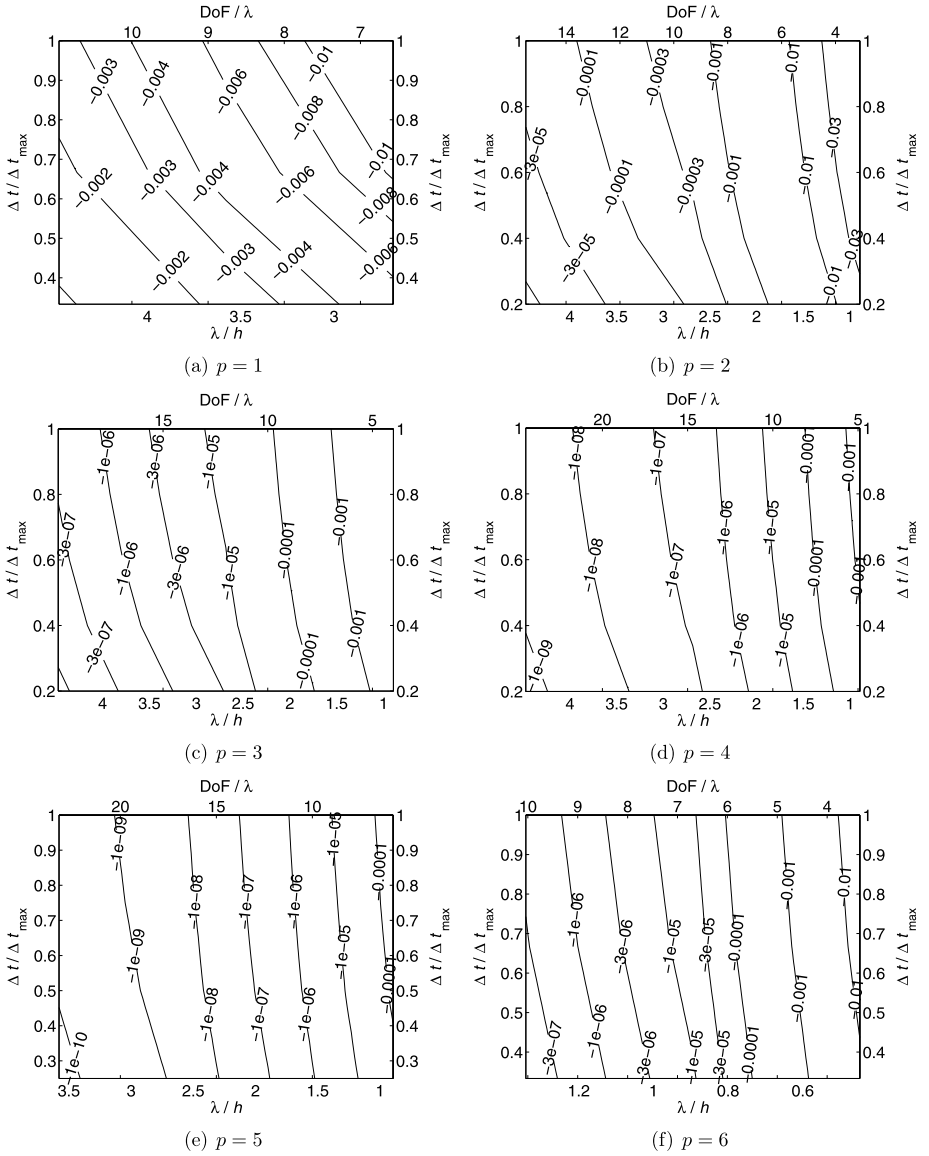

Fig. 6 Dissipation error as a function of wave length per mesh size (λ/h), degrees of freedom per wavelength (DoF/λ) and relative time step ($\Delta t/\Delta t_{\max}$) for polynomial orders $p = 1, 2, 3, 4, 5, 6$ on a uniform mesh

step ($\Delta t/\Delta t_{\max}$). The value $\Delta t/\Delta t_{\max} = 1$ indicates the size of the maximum time step, defined as in (22) in Sect. 4. The contour plots of the dispersion error (or dispersion error) for the one-dimensional analysis with wave number $k = 2\pi$ is shown in Fig. 3 for orders $p = 1, 2$. The same plots for the dissipation error are displayed in Fig. 4. For this range of values the dispersion error is generally at least one order higher than the dissipation error, and it can be improved by both taking smaller time steps and/or refining the spatial grid.

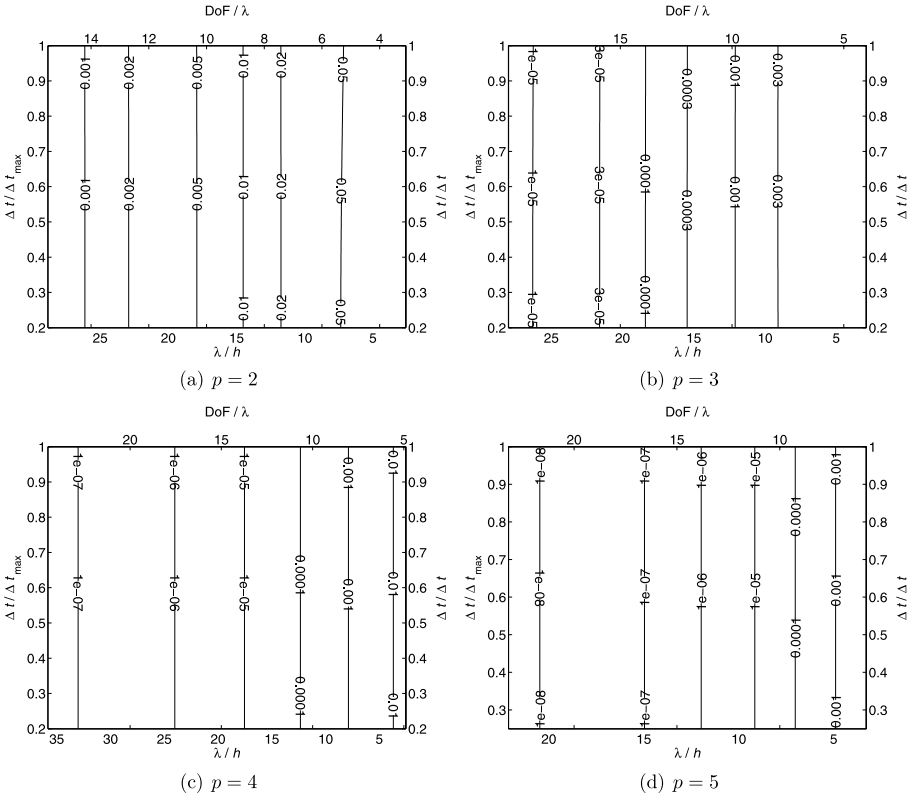

Fig. 7 Absolute value of the dispersion error as a function of wave length per mesh size (λ/h), degrees of freedom per wavelength (DoF/λ) and relative time step ($\Delta t/\Delta t_{\max}$) for polynomial orders $p = 2, 3, 4, 5$ on a non-uniform random mesh

We carry out the same experiment in two dimensions on a uniform grid with wave numbers $k_x = \pi$ and $k_y = 2\pi$ for orders $p = 1, 2, 3, 4, 5$ and $k_x = 2\pi$ and $k_y = 4\pi$ for order $p = 6$. The number of elements used to construct the uniform meshes range from 200 elements to 8 elements for $p = 1, 2, 3, 4$; from 128 elements to 8 elements for $p = 5$; and from 72 elements to 8 elements for $p = 6$. The contour plots of the dispersion and dissipation errors are shown in Fig. 5 and in Fig. 6, respectively. Note that the studied range of wave lengths per mesh size differs significantly from that of the one-dimensional case and occasionally from one another. It can be deduced that the spatial discretisation dominates the dispersion error, which is all the more relevant because the dispersion error is at least one order higher than the dissipation error for all polynomial orders considered. Another important feature—shown in Fig. 9—is the decreasing number of degrees of freedom needed to obtain a given accuracy as we go to higher-order elements. For instance, to attain a dispersion error of 10^{-3}, we need about 14–15 degrees of freedom per wave length for discretisation with second-order polynomials and about six for the discretisation with sixth-order polynomials.

One of the main advantages of DG methods is that they are relatively insensitive to the uniformity of the mesh from the point of view of accuracy and convergence. In order to illustrate that this is the case for the dispersion and dissipation behaviour as well, we perform the same two-dimensional analysis on non-uniform random meshes. To construct the non-

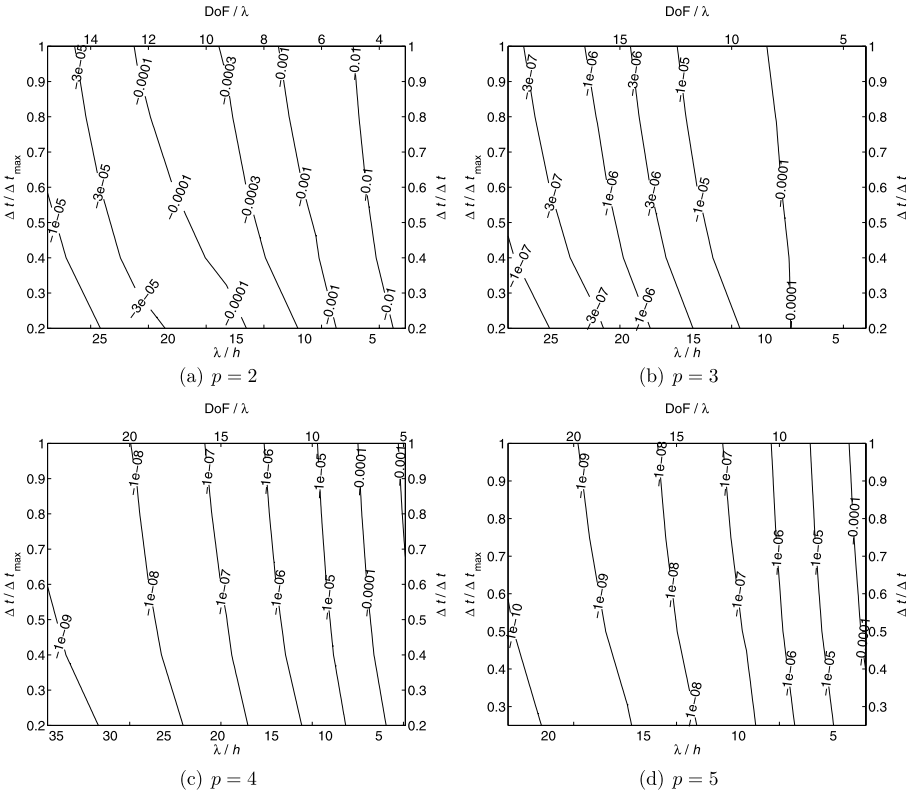

Fig. 8 Dissipation error as a function of wave length per mesh size (λ/h), degrees of freedom per wavelength (DoF/λ) and relative time step ($\Delta t/\Delta t_{\max}$) for polynomial orders $p = 2, 3, 4, 5$ on a non-uniform random mesh

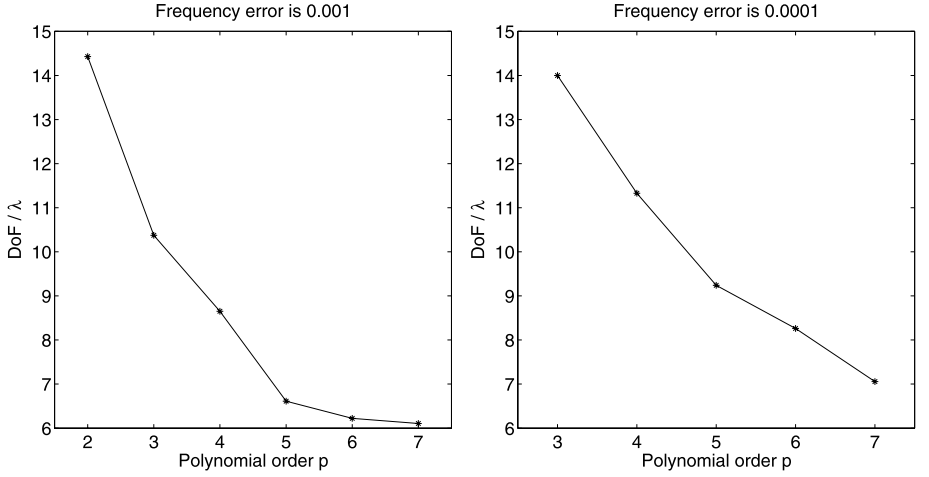

Fig. 9 Degrees of freedom as a function of polynomial order for given dispersion error 10^{-3} and 10^{-4} on uniform meshes

uniform mesh we randomly relocate all inner (ie. not lying on the boundary) vertices of the uniform mesh within the range $[-\frac{h_{\text{ed}}}{3}, \frac{h_{\text{ed}}}{3}]$ in both directions, where h_{ed} is length of the uniformly distributed (one-dimensional) 'boundary' elements. Since the total number of elements in the non-uniform mesh is the same as in the uniform mesh, the values DoF/λ should also be the same (because this is the case 'on average'). However, on the bottom axes the smallest value of h is taken for computing λ/h. The results are shown in Fig. 7 for the dispersion error and in Fig. 8 for the dissipation error. They are qualitatively the same as the corresponding results on uniform meshes, which demonstrates the robustness of the RKDG method.

7 Conclusion

The main purpose of this article has been to study the global dispersion and dissipation errors of a high-order DG spectral element discretisation combined with the high-order SSP-RK time integration. We have shown that by applying the $(p+1)$st-order SSP-RK scheme to a spatial discretisation with pth-order polynomials we can retain $(p+1)$st-order convergence (without preprocessing) in the l_2-norm. Even when the order of the discretisation is increased beyond the accuracy of the fixed-order schemes, the computational work for the SSP-RK scheme is not significantly higher than that of the fixed-order ones. This favourable property can be explained by the much looser time-step restriction. It should be noted, however, that for large systems, the SSP-RK schemes could have a major disadvantage over low-storage RK schemes due to storage requirements. This is because an m-stage SSP-RK scheme requires m storage units per time step, whereas a low storage scheme requires only two storage units per time step.

Through numerical Fourier analysis, it has been demonstrated that the dispersion error of the global scheme is generally at least one order higher than the dissipation error, irrespective of the actual order of the discretisation. It has also turned out that within the studied range of mesh sizes h and time steps Δt we cannot gain anything on the dispersion error by decreasing the time step, i.e. it is worth using the largest one permitted by the CFL condition. This seemingly unusual property can be explained by the fact that the maximum time step allowed by the CFL condition already inflicts a far smaller dispersion error than that of the space discretisation. Using this condition it has also been shown that the convergence rate of the dispersion and dissipation error is far higher, namely $\mathcal{O}(2p)$, than that of the error measured in the l^2-norm. Another important feature of the global scheme is that the number of degrees of freedom to obtain a given accuracy also decreases as the order of the approximation grows.

Acknowledgements This research was supported by the Dutch government through the national program BSIK: knowledge and research capacity, in the ICT project BRICKS (http://www.bsik-bricks.nl), theme MSV1.

Appendix

The exact solution to (23) in the one-dimensional metallic cavity described in Sect. 6.1—with $\kappa = 1, 2$ signifying the two regions filled with different materials—is given by

$$E_\kappa = [-A_\kappa e^{in_\kappa \omega x} + B_\kappa e^{-in_\kappa \omega x}]e^{i\omega t},$$
$$H_\kappa = [A_\kappa e^{in_\kappa \omega x} + B_\kappa e^{-in_\kappa \omega x}]e^{i\omega t},$$

where

$$A_1 = \frac{n_2 \cos(n_2\omega)}{n_1 \cos(n_1\omega)}, \qquad A_2 = \mathrm{e}^{-\mathrm{i}\omega(n_1+n_2)},$$

and

$$B_1 = A_1 \mathrm{e}^{-\mathrm{i}2n_1\omega}, \quad B_2 = A_2 \mathrm{e}^{\mathrm{i}2n_2\omega}.$$

Here $n_\kappa = \sqrt{\varepsilon_\kappa}$ represents the local index of refraction, and the frequency takes the value $\omega = 2\pi/n$ if $n_1 = n_2 = n$ or is found as the solution to the equation

$$-n_2 \tan(n_1\omega) = n_1 \tan(n_2\omega).$$

References

1. Ainsworth, M.: Dispersive and dissipative behaviour of high order discontinuous Galerkin finite element methods. J. Comput. Phys. **198**(1), 106–130 (2004)
2. Ainsworth, M., Monk, P., Muniz, W.: Dispersive and dissipative properties of discontinuous Galerkin finite element methods for the second-order wave equation. J. Sci. Comput. **27**, 5–40 (2006)
3. Bossavit, A.: A rationale for 'edge-elements' in 3-D fields computations. IEEE Trans. Mag. **24**(1), 74–79 (1988)
4. Bossavit, A.: Solving Maxwell equations in a closed cavity, and the question of 'spurious modes'. IEEE Trans. Mag. **26**(2), 702–705 (1990)
5. Carpenter, M.H., Kennedy, C.A.: Fourth order 2N-storage Runge-Kutta scheme. NASA-TM-109112, NASA Langley Research Center, VA (1994)
6. Chen, M.-H., Cockburn, B., Reitich, F.: High-order RKDG methods for computational electromagnetics. J. Sci. Comput. **22/23**, 205–226 (2005)
7. Chen, Q., Babuška, I.: Approximate optimal points for polynomial interpolation of real functions in an interval and in a triangle. Comput. Methods Appl. Mech. Eng. **128**(3–4), 405–417 (1995)
8. Chen, Q., Babuška, I.: The optimal symmetrical points for polynomial interpolation of real functions in the tetrahedron. Comput. Methods Appl. Mech. Eng. **137**(1), 89–94 (1996)
9. Cockburn, B., Shu, C.-W.: Runge-Kutta discontinuous Galerkin methods for convection-dominated problems. J. Sci. Comput. **16**(3), 173–261 (2001)
10. Cockburn, B., Li, F., Shu, C.-W.: Locally divergence-free discontinuous Galerkin methods for the Maxwell equations. J. Comput. Phys. **194**(2), 588–610 (2004)
11. Cockburn, B., Karniadakis, G.E., Shu, C.-W.: The development of discontinuous Galerkin methods. In: Discontinuous Galerkin Methods, Newport, RI, 1999. Lecture Notes in Comput. Sci. Eng., vol. 11, pp. 3–50. Springer, Berlin (2000)
12. Golub, G.H., Van Loan, C.F.: Matrix Computations, 3rd edn. Johns Hopkins Studies in the Mathematical Sciences. Johns Hopkins University Press, Baltimore (1996)
13. Gottlieb, S., Shu, C.-W.: Total variation diminishing Runge-Kutta schemes. Math. Comput. **67**(221), 73–85 (1998)
14. Gottlieb, S., Shu, C.-W., Tadmor, E.: Strong stability-preserving high-order time discretization methods. SIAM Rev. **43**(1), 89–112 (2001)
15. Hesthaven, J.S.: From electrostatics to almost optimal nodal sets for polynomial interpolation in a simplex. SIAM J. Numer. Anal. **35**(2), 655–676 (1998)
16. Hesthaven, J.S.: High-order accurate methods in time-domain computational electromagnetics. A review. Adv. Imaging Electron Phys. **127**(1), 59–123 (2003)
17. Hesthaven, J.S., Teng, C.H.: Stable spectral methods on tetrahedral elements. SIAM J. Sci. Comput. **21**(6), 2352–2380 (2000)
18. Hesthaven, J.S., Warburton, T.: Nodal high-order methods on unstructured grids. I. Time-domain solution of Maxwell's equations. J. Comput. Phys. **181**(1), 186–221 (2002)
19. Hesthaven, J.S., Warburton, T.: High-order nodal discontinuous Galerkin methods for the Maxwell eigenvalue problem. Philos. Trans. Roy Soc. Lond. Ser. A Math. Phys. Eng. Sci. **362**(1816), 493–524 (2004)
20. Hiptmair, R.: Finite elements in computational electromagnetism. Acta Numer. **11**, 237–339 (2002)

21. Houston, P., Perugia, I., Schötzau, D.: Mixed discontinuous Galerkin approximation of the Maxwell operator. SIAM J. Numer. Anal. **42**(1), 434–459 (2004)
22. Hu, F.Q., Atkins, H.L.: Eigensolution analysis of the discontinuous Galerkin method with nonuniform grids. I. One space dimension. J. Comput. Phys. **182**(2), 516–545 (2002)
23. Hu, F.Q., Hussaini, M.Y., Rasetarinera, P.: An analysis of the discontinuous Galerkin method for wave propagation problems. J. Comput. Phys. **151**(2), 921–946 (1999)
24. Jin, J.: The Finite Element Method in Electromagnetics, 2nd edn. Wiley-Interscience, New York (2002)
25. Karniadakis, G.E., Sherwin, S.J.: Spectral/hp Element Methods for Computational Fluid Dynamics, 2nd edn. Numerical Mathematics and Scientific Computation. Oxford University Press, New York (2005)
26. Mohammadian, A.H., Shankar, V., Hall, W.F.: Computation of electromagnetic scattering and radiation using a time-domain finite-volume discretization procedure. Comput. Phys. Commun. **68**, 175–196 (1991)
27. Monk, P.: Finite Element Methods for Maxwell's Equations. Numerical Mathematics and Scientific Computation. Oxford University Press, New York (2003)
28. Monk, P., Richter, G.R.: A discontinuous Galerkin method for linear symmetric hyperbolic systems in inhomogeneous media. J. Sci. Comput. **22/23**, 443–477 (2005)
29. Nédélec, J.-C.: A new family of mixed finite elements in $\mathbf{R}^3$. Numer. Math. **50**(1), 57–81 (1986)
30. Perugia, I., Schötzau, D.: The hp-local discontinuous Galerkin method for low-frequency time-harmonic Maxwell equations. Math. Comput. **72**(243), 1179–1214 (2003)
31. Perugia, I., Schötzau, D., Monk, P.: Stabilized interior penalty methods for the time-harmonic Maxwell equations. Comput. Methods Appl. Mech. Eng. **191**(41–42), 4675–4697 (2002)
32. Sherwin, S.: Dispersion analysis of the continuous and discontinuous Galerkin formulations. In: Discontinuous Galerkin Methods, Newport, RI, 1999. Lecture Notes in Comput. Sci. Eng., vol. 11, pp. 425–431. Springer, Berlin (2000)
33. Taflove, A., Hagness, S.C.: Computational Electrodynamics: The Finite-Difference Time-Domain Method, 2nd edn. Artech House Inc., Boston (2000)
34. Taylor, M.A., Wingate, B.A., Vincent, R.E.: An algorithm for computing Fekete points in the triangle. SIAM J. Numer. Anal. **38**(5), 1707–1720 (2000)
35. Warburton, T., Embree, M.: The role of the penalty in the local discontinuous Galerkin method for Maxwell's eigenvalue problem. Comput. Methods Appl. Mech. Eng. **195**(25–28), 3205–3223 (2006)
36. Williamson, J.H.: Low-storage Runge-Kutta schemes. J. Comput. Phys. **35**(1), 48–56 (1980)
37. Yee, K.S.: Numerical solution of initial boundary value problems involving Maxwell's equation in isotropic media. IEEE Trans. Antennas Propag. **14**(3), 302–307 (1966)